

NRC Publications Archive Archives des publications du CNRC

Quantifying UVC-induced aging of microplastics using a multivariate aging score

Leng, Yingshu; Prezgot, Daniel; Jakubek, Zygmunt J.; Cao, Xudong; Zou, Shan

This publication could be one of several versions: author's original, accepted manuscript or the publisher's version. / La version de cette publication peut être l'une des suivantes : la version prépublication de l'auteur, la version acceptée du manuscrit ou la version de l'éditeur.

For the publisher's version, please access the DOI link below. / Pour consulter la version de l'éditeur, utilisez le lien DOI ci-dessous.

Publisher's version / Version de l'éditeur:

<https://doi.org/10.1007/s10924-026-03796-5>

Journal of Polymers and the Environment, 34, 3, 2026-03-06

NRC Publications Archive Record / Notice des Archives des publications du CNRC :

<https://nrc-publications.canada.ca/eng/view/object/?id=6d719bb8-8f88-4934-b6f1-541526808647>

<https://publications-cnrc.canada.ca/fra/voir/objet/?id=6d719bb8-8f88-4934-b6f1-541526808647>

Access and use of this website and the material on it are subject to the Terms and Conditions set forth at

<https://nrc-publications.canada.ca/eng/copyright>

READ THESE TERMS AND CONDITIONS CAREFULLY BEFORE USING THIS WEBSITE.

L'accès à ce site Web et l'utilisation de son contenu sont assujettis aux conditions présentées dans le site

<https://publications-cnrc.canada.ca/fra/droits>

LISEZ CES CONDITIONS ATTENTIVEMENT AVANT D'UTILISER CE SITE WEB.

Questions? Contact the NRC Publications Archive team at

PublicationsArchive-ArchivesPublications@nrc-cnrc.gc.ca. If you wish to email the authors directly, please see the first page of the publication for their contact information.

Vous avez des questions? Nous pouvons vous aider. Pour communiquer directement avec un auteur, consultez la première page de la revue dans laquelle son article a été publié afin de trouver ses coordonnées. Si vous n'arrivez pas à les repérer, communiquez avec nous à PublicationsArchive-ArchivesPublications@nrc-cnrc.gc.ca.



Quantifying UVC-Induced Aging of Microplastics Using a Multivariate Aging Score

Yingshu Leng^{1,2} · Daniel Prezgot¹ · Zygmunt J. Jakubek¹ · Xudong Cao^{2,3} · Shan Zou¹

Received: 12 December 2025 / Accepted: 13 February 2026
© Crown 2026

Abstract

Microplastics continue to weather as they linger in the environment, yet the roles of polymer type and product formulation in shaping their aging trajectories remain poorly defined. In this work, we examined how commercial polyethylene (PE), polypropylene (PP), and polyethylene terephthalate (PET) microplastics respond to ultraviolet C (UVC) irradiation across doses from 0 to 40 MJ m⁻². Among the three materials, PP changed the most rapidly: its carbonyl index (CI) rose sharply, its melting temperature (T_m) dropped from 157 °C to 141 °C, and its crystallinity (χ_c) declined from 76% to 52%. In contrast, PE and PET showed only modest alterations in their chemical and thermal signatures. Imaging by scanning electron microscopy further highlights the divergence in aging behavior—PP surfaces developed widespread cracks and generated secondary fragments, whereas the other polymers remained comparatively intact. Given that surface oxidation precedes bulk destabilization, we incorporated an infrared (IR)-based surface-crystallinity index (χ_sI) to quantify these early chemical-structural changes. The influence of formulation is investigated using two PP laboratory wastes—transparent centrifuge tubes and blue pipette-tip boxes—both of which show progressive surface cracking, increasing CI, and T_m depression as the UVC dose rises, with the colored material aging faster than the transparent PP. Because aging manifests through several properties that do not evolve in parallel, direct comparisons across polymers and products are challenging. An approach based on principal component analysis integrates CI, T_m , χ_c , and χ_sI into a single quantitative aging score. This unified metric provides an approach for harmonized evaluation of aging levels across polymer types, product formulations, and physicochemical properties. The resulting framework facilitates direct comparisons between materials and provides predictive assessment of microplastic transformation under environmental or laboratory exposure conditions.

Keywords Microplastics · Polymer aging · Oxidation · Weathering · Principal component analysis

Introduction

Microplastics (MPs, < 5 mm) are now ubiquitous in marine, freshwater, soil, and wastewater matrices. They originate from the fragmentation and degradation of larger

plastic debris in the environment through processes such as mechanical abrasion, photodegradation, chemical oxidation, and biodegradation. Once MPs enter aquatic and terrestrial environments, they undergo continuous environmental aging driven by sunlight, oxidants, and mechanical abrasion [1]. Such aging leads to a range of physicochemical property changes, including reduced particle size, surface roughening, formation of carbonyl, hydroxyl, and carboxyl groups, and alterations in thermal behavior and crystalline structures. These transformations modify microplastic transport, aggregation, interactions with contaminants, pollutant sorption, and potential uptake by biota, while also affecting the reliability and sensitivity of detection in environmental samples [1]. Additionally, the pronounced heterogeneity of environmental microplastics in terms of polymer composition, color, morphology, size, and additive content complicates the quantification and comparison of aging, as these

✉ Shan Zou
Shan.Zou@nrc-cnrc.gc.ca

¹ Metrology Research Centre, National Research Council Canada, 100 Sussex Drive, Ottawa, ON K1A 0R6, Canada

² Ottawa–Carleton Institute for Biomedical Engineering, University of Ottawa, 161 Louis Pasteur, Ottawa, ON K1N 6N5, Canada

³ Department of Chemical and Biological Engineering, University of Ottawa, 161 Louis Pasteur, Ottawa, ON K1N 6N5, Canada

characteristics strongly influence degradation pathways, rates, and the expression of physicochemical changes. Most previous studies have focused on differences in aging behaviors among polymer types [2], while systematic quantification of aging variations within a single polymer due to formulation factors (e.g., colorants, additives) remains limited. Despite the rapid growth of MP research, robust quantitative metrics describing “how aged” MP samples are across polymers, product origins, or particle sizes are still lacking. To better quantify and compare microplastic aging, there is a need to standardize studies around robust indicators and analytical techniques that integrate complementary physical, chemical, and mechanical metrics into multivariate factors that more fully describe the progression of aging [3, 4]. Accurately capturing this complexity requires a combination of complementary physical, chemical, and mechanical measurements integrated into multivariate frameworks. Such multi-technique approaches enable fast, high-throughput quantification of aging and improve comparability across studies.

Plastic waste in the environment is subjected to multiple concurrent aging processes, including hydrolysis, photo-oxidation, thermo-oxidation, mechanical degradation, and biodegradation [5], among which photo-oxidative aging is one of the dominant pathways for polyolefins with C–C backbones [6, 7]. Laboratory accelerated aging is therefore widely used to reproduce these complex environmental weathering processes under controlled and reproducible conditions to obtain aged MPs within practical time frames. In contrast, natural weathering often requires months to years to occur and is difficult to standardize across studies [8–10]. Commonly applied laboratory aging approaches include ultraviolet (UV) irradiation (e.g., UVA, UVB, or UVC), thermal and thermo-oxidative exposure, chemically induced oxidation, and biologically mediated aging [10]. Although UVC does not reach the ground level due to atmospheric absorption, its higher photon energy enables more rapid cleavage of surface chemical bonds over short exposure times than UVA or UVB [11], making it an efficient approach for accelerated aging studies. Also, in engineered systems, for example, high-energy UVC at 254 nm from low-pressure mercury lamps is routinely used for disinfection in wastewater treatment plants, indicating that MPs may encounter brief but intense UVC exposures [9, 12]. Consequently, UVC irradiation has become a practical and widely adopted method for producing environment-relevant aged MPs in the laboratory.

UV-aging studies typically expose microplastics either in aqueous media or in air [13, 14]. For hydrophobic polymers such as polyethylene (PE), polypropylene (PP), and polyethylene terephthalate (PET), maintaining homogeneous aqueous suspensions during UV exposure generally requires

surfactants, which stabilize the particles and modify their surface properties and transport behavior [15, 16]. To avoid these surfactant-induced effects and ensure uniform, well-defined irradiation, MPs in this study were exposed to UV in air.

Across UV-based and chemically driven aging pathways, polymers such as PE, PP, and PET undergo oxidation initiated by excited states of photoactive chromophores (e.g., hydroperoxides, carbonyl-containing species, and other impurities/additives) and subsequent free-radical chain reactions. These processes promote the cleavage of covalent bonds, the formation and accumulation of oxygenated functional groups (e.g., carbonyl, hydroxyl, carboxyl species), and progressive surface-to-bulk oxidation [8, 13, 17–21]. These processes increase carbonyl index (CI), alter crystallinity, and promote fragmentation into smaller particles. Beyond polymer type, material formulation and processing history also play an important role in governing aging behavior [22]. For example, the oxidative aging of colored polystyrene (PS) products has been shown to be strongly color-dependent, with white and yellow PS exhibiting the fastest oxidation, reflected by surface O/C ratios and carbonyl signals increasing at rates approximately 1.2–1.8 times and 1.2–5.5 times higher, respectively, compared with red, blue, and black materials [23].

Multiple indicators are therefore used to characterize polymer aging. Changes in thermal behavior, including shifts and broadening of melting temperature (T_m) and variations in crystallinity (χ_c), reflect chain scission and lamellar reorganization, oxidation of amorphous regions, and recrystallization. Li et al. reported a continuous decrease in T_m for LDPE, HDPE, and PP films with increasing UVB exposure, attributed to reduced molar mass and lamellar disruption [24]. While Canopoli et al. observed approximately two-fold increases in crystallinity for landfill-aged PE and PP relative to fresh plastics, as determined by differential scanning calorimetry (DSC) analysis [25]. On the chemical side, the CI has long been used as an indicator of photo-oxidation in polyolefins [26], defined as the ratio of the infrared absorption of carbonyl groups at $\sim 1720\text{ cm}^{-1}$ relative to a reference peak. Consistent increases in CI have been documented across UV-aging studies. For instance, the CI value in PP mask materials increased from 0.14 to 0.17 under mild conditions to approximately 0.45 under photoaging at elevated temperature [27]. Similarly, Gao et al. observed a continuous increase in CI for PE and PP aged microplastics under UVA in seawater [13], further supporting that CI rises reflecting progressive photo-oxidation.

In addition to the carbonyl groups, other infrared absorption bands provide useful indicators of aging, including the broad hydroxyl stretch ($3100\text{--}3500\text{ cm}^{-1}$) and the C–H band at 888 cm^{-1} associated with vinylidene groups, each of which

can be expressed as an index relative to an unchanging reference peak [28]. Crystallinity can also be inferred through IR spectroscopy. In PP, certain bands respond to crystalline content; for example, the 998 cm^{-1} band increases with crystallinity, whereas reference bands such as 974 cm^{-1} remain largely invariant [29]. Therefore, the intensity ratio of the $998/974\text{ cm}^{-1}$ peak pair provides a measure proportional to crystallinity. Lanyi et al. used this approach alongside DSC and X-ray diffraction (XRD) to assess bulk and surface crystallinity gradients in PP [30]. Building on this approach, we use the same crystallinity-sensitive peak ratio to establish the surface crystallinity index (χ_{sI}) by employing attenuated total reflectance Fourier-transform infrared spectroscopy (ATR-FTIR). Since ATR-FTIR has an estimated penetration depth of $\sim 2\text{ }\mu\text{m}$, the measurement is considered more sensitive to surface crystallinity than to bulk crystallinity, compared with DSC.

While the availability of these physical and chemical indicators makes it challenging to compare results across studies, the absence of standardized approaches that harmonize aging metrics across polymer types, product sources, and particle sizes further complicates the task. Individual measurements, such as CI, T_m , χ_c , χ_{sI} , and size reduction capture only isolated facets of aging, and different properties often evolve at non-parallel rates. As a result, environmental assessment and risk evaluation require integrated, quantitative metrics that reflect the overall degree of aging in a manner applicable across polymers and formulations [3, 4].

Multivariate statistical analysis offers a route to unify disparate measurements and evaluate their contributions to natural or accelerated aging. Principal component analysis (PCA) has been used to reduce dimensionality, visualize multivariate trends, and classify or regress complex datasets [31]. By transforming data using covariance matrices, PCA weights each feature according to its contribution to overall variance, highlighting the most influential variables. In polymer and plastics research, it has been applied to polymer classification [32], analysis of IR spectroscopy [33], interpretation of mass spectrometry data [34], and evaluation of changes in physicochemical properties [35]. Integrating thermal, chemical, and structural measurements in a multivariate framework allows these complementary aging indicators to be assessed together. It helps capture the complex, non-parallel changes that occur across polymer types and formulations. To further confirm how each variable contributes within this framework, Shapley additive explanations (SHAP) were used to analyze the relative influence of each feature on the aging score. SHAP is derived from the Shapley value, which is a method in cooperative game theory for distributing a total value among cooperating players based on their individual contributions. It has been widely

adopted in machine learning as a model-agnostic approach for explaining the contribution of individual features to the outputs of a model [36].

Notwithstanding these advances, standardized and quantitative frameworks that capture the multidimensional nature of microplastic aging across polymer types, product formulations, and particle sizes remain lacking. To address this gap, we develop a fast, high-throughput, multi-technique approach that combines complementary thermal, chemical, and structural measurements into a single, interpretable aging score. Using this framework, we monitored the aging progression of micro-sized PE, PP, and PET, as well as MPs generated from laboratory waste, under controlled UVC irradiation in air. The resulting quantitative aging score enables direct comparison of aging level across polymers and product sources, treating polymer aging as a measurable, integrative parameter and providing a unified system to answer “how much aging has occurred?” across diverse microplastic samples.

Materials and Methods

Microplastics Preparation

Commercial plastic powders: PE (average size $9\text{ }\mu\text{m}$) and PP (average size $38\text{ }\mu\text{m}$) were purchased from Polysciences (Warrington, PA), and PET (average size $20\text{ }\mu\text{m}$) was purchased from Chemazone (Leduc, AB). Two PP-based lab consumables used in this study were: (i) PP centrifuge tubes (PPCT, transparent) and (ii) PP pipette boxes (PPPB, opaque blue). Each material was manually cut into 2–4 mm flakes using scissors. Flakes were dispersed in 200 mL of Milli-Q water with 5 mL of ethyl alcohol (95%, Commercial Alcohols Inc., Brampton, ON, Canada) to aid dispersion. The suspension was then subjected to mechanical fragmentation using a laboratory blender operated at high speed for 30 min, following a pulsed protocol of 30 s blending and 10 s pause to produce fragmentation while preventing overheating. The suspensions were filtered through a $5\text{ }\mu\text{m}$ stainless-steel mesh, and the retained material was oven-dried at $50\text{ }^\circ\text{C}$ to constant mass. Dried particles were sieved through stainless-steel meshes to obtain different size classes. Particles smaller than 5 mm were further subdivided into fractions differing by approximately one order of magnitude using mesh sizes of 500, 250, and $125\text{ }\mu\text{m}$, yielding the 250–500 μm and $<125\text{ }\mu\text{m}$ fractions. Accordingly, three PP size groups were defined for subsequent experiments: large (L), 2–4 mm in edge length; medium (M), $351\pm 181\text{ }\mu\text{m}$ (average \pm SD); and small (S), $97\pm 44\text{ }\mu\text{m}$ (average \pm SD).

UVC Aging Process

Approximately 150 mg of each polymer powder or polypropylene (PP) microplastic fraction was placed into individual quartz vials (Aireka Scientific Co., Hong Kong, P.R. China), with nine vials typically irradiated per batch. Samples were exposed to 254 nm UVC in air using 18 W low-pressure mercury lamps (Rayonet, Branford, CT) arranged circumferentially around the vials to ensure uniform irradiation [37, 38]. Temperature was continuously monitored at the center of the sample plane during exposure and remained between approximately 50 and 56 °C. All experiments were conducted under ambient atmospheric conditions. UVC irradiance at the sample plane was measured prior to each experiment using a radiometer (Newport, Irvine, CA). After reaching a stable output, power (P , mW) was recorded radially from the center at twelve angles in 30° increments and averaged to obtain the effective power. Irradiance (P/A , W m⁻²) was calculated as the measured power (P) divided by the active sensor area (A) (8.3×10^{-5} m²). The cumulative UVC radiant exposure (dose) (H , MJ m⁻²) was obtained as:

$$H = \frac{P t}{A} \times 10^{-6}$$

where t is the exposure time (s). The factor 10^{-6} converts joules to megajoules.

UVC irradiation was applied as an energetically accelerated aging method, in which high-energy photons were used to increase the rate of photo-oxidative degradation under controlled conditions. A maximum cumulative dose of 60 MJ m⁻² was applied, which corresponds to a few months to about one year of natural UV exposure in terms of radiant energy (typically on the order of ~190–340 MJ m⁻² per year, depending on the location) [39–41]. Four to six aliquots (~25 mg each) were taken from each vial at predefined intervals to monitor changes at progressively increasing UVC doses.

Surface Morphology Observation and Size Distribution Analysis

Surface morphology of all MP materials was examined using a Phenom Pro desktop scanning electron microscopy (SEM, Thermo Scientific, Phoenix, AZ). SEM imaging was conducted at 5 kV and 2800× magnification. Particle size for the commercial polymers was measured from SEM images. In contrast, PPCT and PPPB particles were measured from optical images acquired using an ECHO Revolve R4 microscope (Discover Echo, San Diego, CA) with a 4× objective. Ten randomly selected fields of view were analyzed, yielding a total of 300 particles to minimize sampling bias. Image

analysis was performed in ImageJ (National Institutes of Health, Bethesda, MD).

Since particles exhibited irregular shapes, size was represented using the mean Feret diameter. The Feret diameter is the distance between two parallel tangents drawn along a specified direction; it is commonly used to characterize changes in average molar mass during polymer degradation [42]. In this study, the mean Feret diameter was calculated as the average of the maximum and minimum Feret diameters for each particle.

Melting Temperature and Crystallinity Analysis

Differential scanning calorimetry (DSC Q2000, TA Instruments, New Castle, DE) equipped with a refrigerated cooling system (RCS90, TA Instruments, New Castle, DE) was used to characterize thermal properties of the polymer samples. Dry plastics (2–5 mg) were placed into Tzero aluminum pans, sealed with Tzero lids using a Tzero DSC sample encapsulation press (all from TA Instruments, New Castle, DE). Crucible and sample masses were measured using an XPE-205 analytical balance (Mettler-Toledo, Oakland, CA) with a readability of 0.01 mg. The DSC equipment was calibrated periodically during the measurements using indium standards.

Measurements were performed under modulated differential scanning calorimetry (MDSC) mode to resolve reversing (e.g., melting) and non-reversing (e.g., decomposition) thermal events [43, 44]. A constant heating rate of 10 °C/min was used, with a temperature modulation amplitude of 0.796 °C every 60 s. Temperature ranges were selected according to polymer type, with PE heated from 50 to 150 °C, PP from 50 to 200 °C, and PET from 150 to 300 °C. A nitrogen purge of 50 mL/min was maintained throughout the analysis. Thermograms from the first heating ramp were used for data interpretation.

To identify the plastic melting temperature (T_m) in the samples, the ‘peak maximum’ feature in the Universal Analysis 2000 (version 4.7.0.2, TA Instruments, New Castle, DE) was employed to locate the peaks of T_m from the first heating cycle of the reversed thermogram. The peak determination follows the polymer-specific onset and offset windows of 63–130 °C for PE, 95–170 °C for PP, and 185–270 °C for PET, with an error of ± 1 °C.

To determine crystallinity (χ_c), the melting peak area from the first heating cycle of the reversed thermogram was integrated using linear baseline correction, with the onset and offset temperatures set to the same values used for T_m determination for PE, PP, and PET. The crystallinity is calculated by dividing the obtained peak area, corresponding to the heat of fusion (ΔH_m), by the heat of fusion value for

100% perfectly crystalline polymer (ΔH_0 , PE: 297 J/g; PP: 207 J/g, PET: 140 J/g) [45].

$$\%Crystallinity (\chi_c) = \frac{\Delta H_m}{\Delta H_0} \times 100\%$$

Carbonyl Index and Surface Crystallinity Index Analysis

ATR-FTIR was performed using a Bruker InvenioX FTIR equipped with a Bruker Platinum ATR accessory containing a diamond element (Bruker Optics, Ettlingen, Germany). Measurements were carried out by dispersing a small amount of powder onto the ATR element or a single piece of plastic for the large samples, and pressing against the element. This was repeated 3 times for each measurement. FTIR spectra were collected from 600 to 4000 cm^{-1} at a resolution of 4 cm^{-1} with a coaddition of 32 scans.

All spectra were pre-processed by asymmetrically reweighted penalized least squares (arPLS) [46] using the pybaselines Python package (Python 3.12.3) [47]. The carbonyl index was used as an indicator of oxidation extent by comparing the peak area (A) of the carbonyl peak (1660–1860 cm^{-1}), and a reference peak which was agnostic to photooxidation, and varied by polymer:

$$Carbonyl\ Index\ (CI) = \frac{A_{1720\ \text{cm}^{-1}}}{A_{reference}}$$

Peak areas were obtained over a local baseline established by first subtracting a line between the first and last points of the integration region, then integrating absorbance via the trapezoid method. The reference peaks were at 1455 cm^{-1} for PP and 1460 cm^{-1} for PE [9]. For PET, the ester backbone already gives a strong intrinsic carbonyl band [48], so the carbonyl peak was integrated over 1620–1860 cm^{-1} , with the reference peak at 1410 cm^{-1} .

The change in surface crystallinity index ($\chi_s I$) of PP, evaluated by ATR-FTIR, was determined as the ratio of the peak heights (h) at 998 cm^{-1} and 974 cm^{-1} , with a common baseline.

$$Surface\ Crystallinity\ Index\ (\chi_s I) = \frac{h_{998\ \text{cm}^{-1}}}{h_{974\ \text{cm}^{-1}}}$$

Aging Score Framework

A metric summarizing the overall change in observed measurements, T_m , χ_c , CI, and $\chi_s I$, was calculated through a multivariate statistical approach based on principal component analysis (PCA). The procedure for obtaining this value was as follows: each measured quantity (feature) was taken

as the change in each aged sample relative to the control (unaged) sample, yielding $\Delta\text{feature}$. Because the features have different scales and units, all variables were normalized using standard z-score normalization on a per-feature basis. PCA was applied to the scaled data using scikit-learn (v1.7.1) on Python 3.12.3. Each sample becomes represented by a principal component score (z), described in n dimensions, where $n \leq$ the number of features, i.e., $z = (z_1, z_2, \dots, z_n)$. A baseline point was established by taking the mean of the principal component scores of the control samples, which collapsed to a single PC score since $\Delta\text{features}$ were used, and all initial values for the control samples were set to 0. A weighted Euclidean distance between the PC score of any given sample (z_i) and the PC score of the baseline point (z_0) was calculated, where each principal component (z_n) was weighted by its explained variance ratio (λ_n). The aging score was calculated as:

$$Aging\ Score = \sqrt{\sum_{n=1}^k \lambda_n (z_{i,n} - z_{0,n})^2}$$

where $z_{i,n}$ and $z_{0,n}$ represent the scores of the n -th principal component for the sample and baseline reference, respectively, λ_n is the explained variance ratio of the n -th principal component, and k denotes the number of principal components retained. The baseline reference (z_0) was defined as the centroid of pristine microplastic samples in the PCA space.

The impact of each feature on the aging score was examined using Shapley values. Shapley additive explanations (SHAP) were applied to the aging score function using a kernel approach via the SHAP package (v0.48).

Data Analysis

Data analysis was performed to evaluate aging-induced changes in the chemical, thermal, and morphological properties of the polymers. All measurements were performed using three independent replicate samples ($n=3$). Reported values are presented as mean \pm standard deviation (SD), and error bars shown in the figures represent the corresponding standard deviation, unless otherwise stated.

Linear regression analysis was performed using GraphPad Prism 10.6.1 (GraphPad Software, San Diego, CA) to evaluate aging-induced trends in carbonyl index, melting temperature, and crystallinity as a function of UVC exposure. An ordinary least-squares linear model with an unconstrained intercept was fitted to individual replicate data for each polymer. The significance of exposure-dependent trends was assessed by testing whether the regression slope differed from zero using the associated t-test. Differences in trend magnitude among descriptors were evaluated by

comparing regression slopes with an F-test; $p < 0.05$ was considered significant.

Statistical analyses were applied where discrete group comparisons were appropriate. In particular, particle size distributions between pre- and post-UVC samples were compared using the nonparametric Mann-Whitney test, with $p < 0.05$ considered significant.

Results and Discussion

Polypropylene Undergoes the Most Pronounced UVC Aging

The aging responses of PE, PP, and PET to UVC irradiation were assessed using chemical, thermal, and morphological analyses. Differences in monomer composition and polymer architecture strongly influenced the extent of degradation. PE and PP are polyolefins with saturated hydrocarbon backbones, whereas PET is a polyester with an aromatic ester backbone. These structural variations determine how readily a polymer reacts with oxygen, undergoes chain scission, and experiences lamellar order or surface changes.

ATR-FTIR was used to track oxidation, particularly the formation of carbonyl groups. ATR-FTIR spectra of PE, PP, and PET show increasing carbonyl-band intensity with higher UVC exposure (Fig. 1a–c), and integration of this band yields a rising carbonyl index (CI), confirming the occurrence of oxidation. Because the carbonyl peak at 1720 cm^{-1} represents a mixture of photo-oxidation products, integration of the peak area was employed rather than peak height to better quantify the full extent of photochemical changes [28]. For PE and PP, the carbonyl region appears as a developing band on an otherwise low-carbonyl baseline, such that the emergence and integrated area of the 1720 cm^{-1} region are straightforward indicators of new photo-oxidation products. For PET, by contrast, the ester carbonyl is an inherent feature of the backbone; the 1720 cm^{-1} region therefore represents a mixture of intrinsic and newly formed carbonyl species, which limits the interpretability and quantitative comparability of CI across polymers. Although alternative PET oxidation proxies, such as acid carbonyl bands and hydroxyl stretching modes, have been reported in the literature, CI is retained here to maintain a consistent oxidation-related descriptor across polymers within this study.

For each polymer, CI increases approximately linearly with dose over the tested range (Fig. 1g), enabling a simple comparison of oxidation rates based on the CI-dose slope. Using the same integration approach and polymer-specific reference peaks, we find that PP has the steepest CI-dose slope, indicating the most rapid accumulation of carbonyl functionality under identical irradiation conditions. PET

exhibits a higher slope than PE, despite the visual spectral comments above; this apparently paradoxical outcome likely reflects normalization artifacts in PET because of its pre-existing ester carbonyl signal and the increased sensitivity of the CI calculation to baseline or reference-peak variability in that polymer. Importantly, CI values are measured relative to polymer-specific reference peaks and therefore are not absolute cross-polymer concentrations; the slope metric is the appropriate comparator for oxidation susceptibility across polymers in this dataset [49].

The spectral trends are consistent with UVC-driven formation of oxygen-containing groups via radical pathways (peroxy and alkoxy intermediates) and subsequent chain-end or backbone functionalization [50, 51]. The comparatively strong spectral response of PP reflects its higher density of tertiary C–H sites and chromophoric susceptibility to radical formation relative to PE. At the same time, the intrinsic carbonyl baseline of PET alters how newly formed oxidation products manifest in spectra [52]. In this study, PET degraded more slowly under UVC aging in air because PET degradation primarily proceeds via ester-bond cleavage and the formation of carboxylic end groups via photo-induced and hydrolysis-assisted processes in water [53]. Those hydrolytic pathways are limited in dry UVC-in-air conditions.

Upon UV aging, peroxide formation cleaves covalent bonds, inducing chain scission and generating low-molecular-weight fragments or monomeric species, which in turn affect the thermal stability of the plastic [5]. DSC is commonly used to characterize such thermal behavior [54], as changes in molecular mobility and chain packing manifest as shifts or broadening in thermal transitions such as melting temperature (T_m). As shown in Fig. 1d–f, PP exhibited a clear shift and broadening of the melting endotherm, with T_m falling from $157\text{ }^\circ\text{C}$ to $141\text{ }^\circ\text{C}$. Among the three polymers, PP showed a significantly faster T_m decrease with UV dose than PE and PET ($P < 0.0001$), whereas PE and PET showed only modest changes and remained near their original T_m over the same dose range (Fig. 1h).

Bulk crystallinity changes (χ_c) derived from MDSC melting enthalpy (Fig. 1i) further confirm that PP experiences the largest crystallinity loss (76% to 52%), consistent with lamellar disruption and partial loss of ordered crystalline domains. This χ_c reduction in PP is significantly greater than that observed for PE and PET ($p < 0.05$). The observed PP thermogram evolution (T_m depression and χ_c loss) is consistent with chain scission disruption of lamellar orders. At the same time, shorter chain fragments can also recrystallize into less perfect lamellae, with broadened and shifted melting behavior [55, 56]. The near-stability of PE and PET thermograms suggests that UVC-induced chain scission or structural reorganization is either slower in these polymers

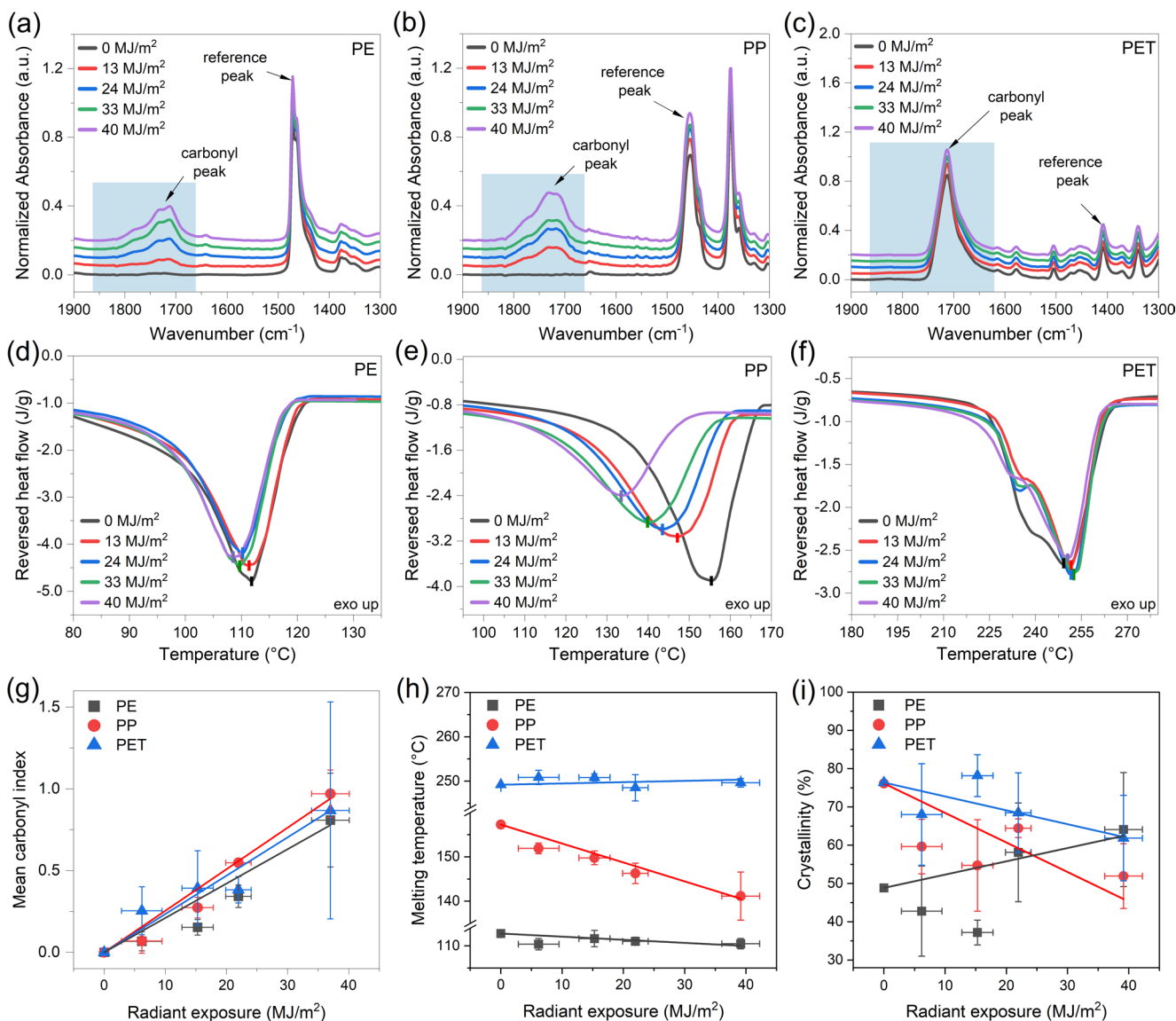


Fig. 1 Chemical and thermal property changes of PE, PP, and PET pre- and post-UVC irradiation (0 and 40 MJ m⁻²). (a–c) ATR-FTIR spectra in the 1900–1300 cm⁻¹ region and (d–f) MDSC thermograms of PE, PP, and PET under UVC exposure up to 40 MJ m⁻². The reversed heat flow is presented with the exothermic direction oriented upward

(exo up). Changes in carbonyl index (g), melting temperature (h), and crystallinity (i) of PE, PP, and PET under UVC exposure up to 40 MJ m⁻². The solid lines correspond to linear fits applied to each dataset. The error bars represent the standard deviation calculated from three replicate samples ($n=3$)

or predominantly occurs at the surface, below the bulk-sensitive DSC detection threshold. Overall, the divergent thermal responses indicate that UVC exposure more strongly perturbs the bulk crystalline structure of PP than that of PE or PET under the experimental conditions used.

The observed thermal changes imply that chain scission and lamellar disruption are accompanied by surface-level manifestations, such as cracking and fragmentation, which can be directly visualized. SEM images reveal polymer-specific surface responses: PP develops pronounced cracking and secondary fragments after UVC exposure, PE shows slightly surface flaking, and PET remains largely

unchanged (Fig. 2a). These morphological observations are complemented by particle size analysis, which provides an additional indicator of microplastic aging, as UV-induced embrittlement and cracking can lead to fragmentation into smaller particles [57]. Consistent with the morphology changes in SEM images, post-UVC size distributions shifted toward smaller particles for PP and PET (Fig. 2b–d), with the largest decrease observed for PP from (38.4 ± 19.7) μm to (16.4 ± 11.5) μm (Fig. 2c).

This pattern aligns with previous reports showing that PP undergoes more advanced surface cracking and oxidation than PE under comparable UV irradiation [58]. The observed

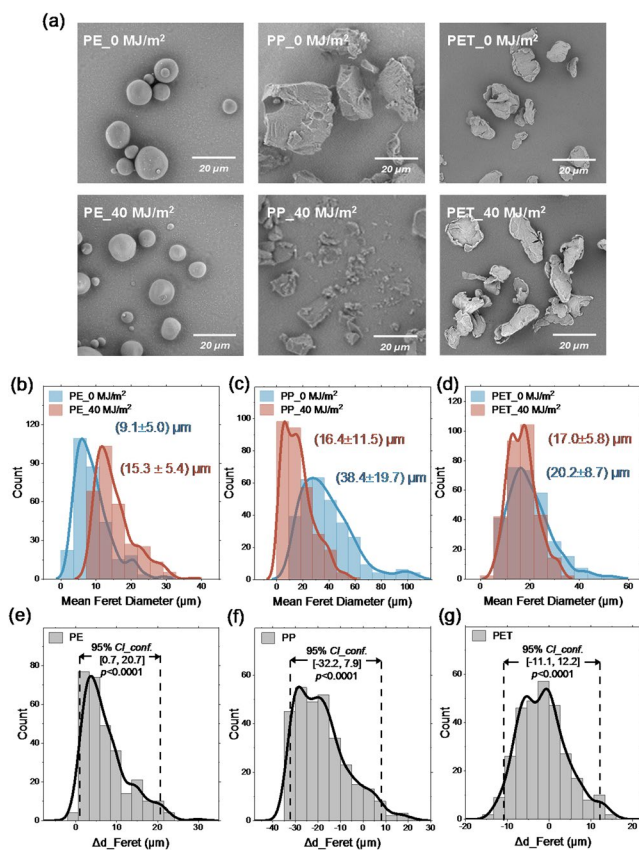


Fig. 2 Morphology changes and particle size distributions of PE, PP, and PET pre- and post-UVC irradiation (0 and 40 MJ m⁻²). **(a)** SEM images of PE, PP, and PET pre- and post-UVC irradiation. **(b–d)** Histograms with overlaid kernel density curves showing the size distributions of 300 particles for each polymer, with mean and standard deviation indicated. **(e–g)** Distribution of size shifts for PE, PP, and PET post UVC irradiation. Dashed lines indicate the 95% confidence intervals (*CI_conf*), and statistical analysis using the Mann–Whitney test shows highly significant differences between pre- and post-UVC samples ($p < 0.0001$ for all cases)

fragmentation is consistent with a photo-oxidative degradation mechanism, in which UV-induced chain scission and surface embrittlement generate fractures that evolve into crack networks and secondary fragments. These fragments act as stress concentrators, further accelerating size reduction [58, 59]. To facilitate a direct, polymer-independent comparison of UV-induced fragmentation, we analyzed the size shift between pre- and post-UVC samples rather than the raw size distributions. As shown in Fig. 2e–g, nonparametric tests confirmed significant pre/post differences for all plastics (Mann–Whitney, $p < 0.0001$), with PP exhibiting the largest median decrease and a broader negative tail in the size-shift distribution (Fig. 2f), indicating both a greater extent and higher heterogeneity of fragmentation.

For more UV-resistant polymers like PET, cracking and fragmentation were not dependable visual indicators under the applied conditions, reinforcing the need to rely

on chemical and thermal metrics to capture aging [60, 61]. These results show that PP displays internally consistent chemical, thermal, and physical responses indicative of advanced aging, PE exhibits limited oxidation and early surface changes with weak thermal effects, and PET remains comparatively resistant within the tested UVC dose range. It should be noted that detailed formulations of the commercial plastic powders were not provided by the manufacturers. Therefore, the observed aging behavior reflects the combined effects of polymer chemistry and formulation-specific additives, rather than intrinsic polymer susceptibility alone.

Chemical and Thermal Characteristics of Aged PP

The aging rate of polymers is determined not only by their intrinsic molecular structure but also by additives and the polymerization or processing techniques used during manufacture to enhance material performance. In commercial plastics, stabilizers and antioxidants are commonly incorporated to improve color, processability, and mechanical properties, thereby increasing resistance to degradation [5, 62]. Among these, colorants can strongly influence environmental durability by modifying photodegradation pathways, and the loss of pigments from the bulk can further weaken the polymer [63, 64]. To explore how these formulation factors affect UVC-induced aging, two representative laboratory plastic wastes were selected: transparent disposable polypropylene centrifuge tubes (PPCT) and opaque blue pipette tip boxes (PPPB). Additionally, the size, shape, and thickness of plastic items strongly influence their fragmentation patterns and aging behavior. This is further illustrated by cross-sectional oxidation profiles, in which ATR-FTIR measurements taken at different depths in a larger-size fraction of PP materials show higher carbonyl peak areas near the surface and progressively lower levels toward the interior (Fig. S1), indicating that oxidation proceeds inward from the exterior. Such surface-initiated oxidation implies a possible size dependence. Also, smaller particles (< 500 nm), owing to their higher surface-area-to-volume ratios, are generally more susceptible to degradation, as enhanced surface exposure accelerates oxidative reactions [65, 66].

Bulk thermal properties, assessed by MDSC, demonstrated size-dependent structural effects. With increased UVC exposure, the leftward shift of the melting peaks and the reduction in peak area indicate decreased T_m and χ_c (Fig. S2), consistent with chain scission, lamellar thinning, and partial loss of order domains, which reduce the thermal stability of the semi-crystalline structure [67, 68]. A pronounced size effect was observed in T_m (Fig. 3a and e), where small-sized PPCT-S and PPPB-S exhibited the largest T_m decreases (18 °C and 23 °C, respectively), followed

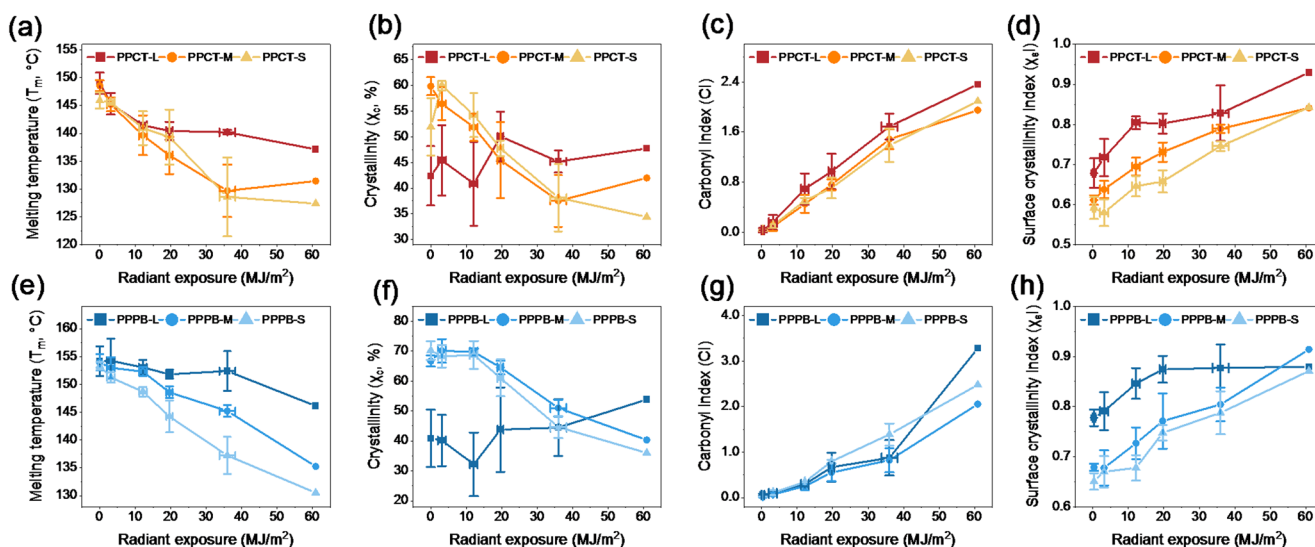


Fig. 3 Changes in melting temperature (T_m), crystallinity (χ_c), carbonyl index (CI), and surface crystallinity index ($\chi_s I$) of polypropylene lab consumables under increasing UVC dose. (a–d) PPCT and (e–h) PPPB. Error bars represent the standard deviation from triplicate sam-

ples ($n=3$). Data points at 60 MJ m^{-2} correspond to an exploratory, late-stage aging condition and were obtained from a single sample; therefore, error bars are not shown for this exposure

by medium and large fractions ($S > M > L$). This size dependence was particularly clear for PPPB, where the small fraction showed a much stronger T_m depression ($P < 0.0001$), and a more moderate but still significant effect for PPCT ($p < 0.05$), likely due to their higher surface area-to-volume ratio, greater oxidized surface fraction, and increased susceptibility to lamellar disruption, in agreement with previous microplastics aging studies [57].

Changes in χ_c followed a more complex trend. As shown in Fig. 3b and f, the medium and small fractions of both PPCT and PPPB showed overall χ_c reduction after 60 MJ m^{-2} UVC exposure, confirming progressive disruption of crystalline lamellae [68]. Across the full exposure range, these χ_c changes were statistically significant for both PPCT and PPPB ($p < 0.0001$). In the large size fraction, PPCT-L showed a slight increase in χ_c during early exposure at 3 MJ m^{-2} before decreasing at 12 MJ m^{-2} , followed by partial recovery at 20 MJ m^{-2} and gradual decline at higher doses. In comparison, PPPB-L exhibited an initial decrease at a low UVC dose of 12 MJ m^{-2} , followed by an increase at higher exposure levels. This transient recrystallization aligns with literature-reported mechanisms in which initial chain scission allows short-chain lamellae to reorganize before further oxidative degradation dominates [67]. The medium- and small-size fractions tended to exhibit smoother, near-linear decreases in χ_c , and no evident size-dependent pattern was observed, suggesting that once surface oxidation reaches a critical extent, further crystallinity loss proceeds more uniformly in smaller particles.

ATR-FTIR analysis revealed a systematic increase in CI with increasing UVC irradiation exposure across all

polypropylene materials and three size classes, demonstrating a clear dose-dependent oxidation response (Fig. 3c and g). Linear analyses of CI versus dose revealed material-specific trends: for the medium and small size fractions, PPCT and PPPB particles exhibited nearly identical CI growth, whereas in the large size fraction, PPPB displayed a sharp increase at more prolonged exposure (60 MJ m^{-2}), suggesting an accelerated oxidation process. Interestingly, for the surface crystallinity index, $\chi_s I$ showed an overall increasing trend across all size fractions (Fig. 3d and h), in contrast to the trends observed in χ_c . While χ_c decreases as bulk lamellae are disrupted, $\chi_s I$ increases because the surface chain scission generates shorter and more chain segments that are more capable of reorganizing into surface-localized ordered regions [69]. This contrasting behavior highlights the importance of distinguishing bulk versus surface-sensitive metrics when assessing polymer aging. For PPPB, however, the increase in $\chi_s I$ began to level off beyond 20 MJ m^{-2} , likely due to surface oxidation, which reduces chain mobility and limits further ordering. Notably, PPPB exhibited significant size dependence in both CI ($p < 0.01$) and $\chi_s I$ ($p < 0.001$), whereas no significant size dependence was detected for PPCT. The discrepancy between PPPB and PPCT may further reflect formulation differences, as pigments and stabilizer packages are known to strongly modulate PP degradation depth profiles, which are often governed by oxygen-diffusion-limited surface reactions [70]. Additionally, given the surface-sensitive nature of ATR-FTIR measurements, which probe approximately the outer $2 \mu\text{m}$ of samples, the calculated CI and $\chi_s I$ mainly represent surface oxidation that can be similar across sizes.

Surface Morphology and Particle Size Evolution of PP

Building on the chemical and thermal changes, the two PP materials with distinct additive compositions and coloration provide a basis for comparing their morphological changes and particle-size evolution under controlled UVC exposure.

The surface morphology and size change of PPCT and PPPB in large (L), medium (M), and small (S) size fractions under UVC are shown in Fig. 4. For the large fractions (PPCT-L and PPPB-L), initially smooth and featureless surfaces developed dense crack networks after UVC irradiation (Fig. 4a), indicating that UV-induced degradation affected the entire exposed surface and that the materials

had become sufficiently embrittled for mechanical stresses to be relieved through crack formation [59]. Notably, PPCT-L tended to form finer and more continuous crack patterns, whereas PPPB-L exhibited wider and shallower cracks. This difference is likely associated with formulation-level variations, including pigment incorporation and stabilizer packages, which may influence both the depth and uniformity of oxidation as well as the distribution of mechanical stresses within the surface layer [17, 64, 71], although contributions from other formulation- or history-dependent factors cannot be excluded.

In the medium-size fraction (M, Fig. 4b), PPCT-M also displayed apparent intergranular cracks after UVC irradiation, accompanied by an 86% decrease in mean Feret

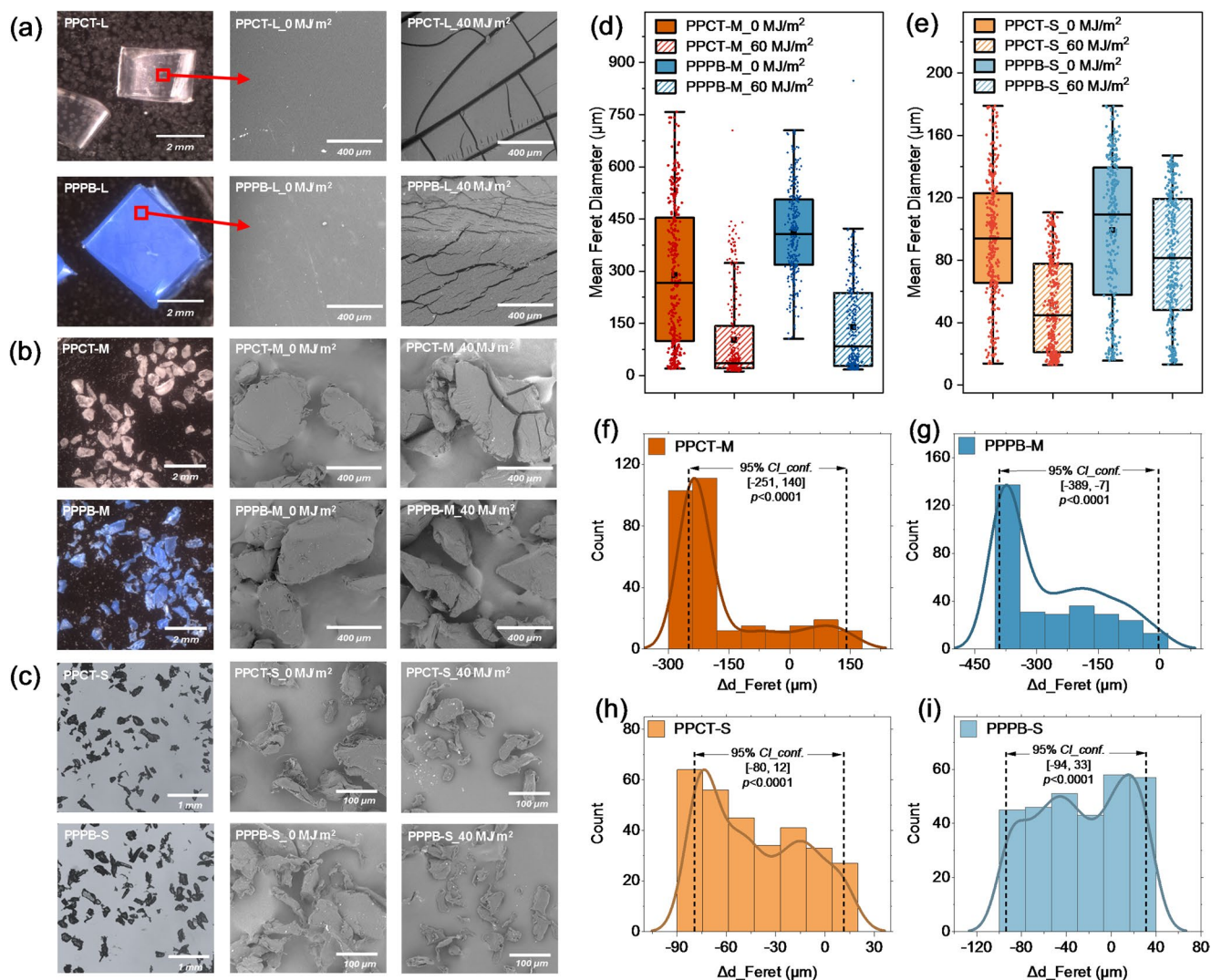


Fig. 4 Morphology and size distribution change. SEM images of PPCT, PPPB in (a) large, (b) medium, (c) small sizes pre- and post-UVC (0 and 60 MJ m⁻²) exposure. (d–e) Box plots of size distributions of PPCT and PPPB samples in medium and small sizes. Mean values (■), medians (—), interquartile range (25–75%), and minimum-maximum values ($n=300$) are presented. (f–i) Distribution of size shifts

for PPCT-M, PPPB-M, PPCT-S, and PPPB-S post UVC irradiation. The dashed line represents the 95% confidence intervals (CI_{conf}), and statistical analysis using the Mann–Whitney test indicated highly significant differences between pre- and post-UVC (0 and 60 MJ m⁻²) samples ($p<0.0001$ for all cases)

diameter from a median of 266 μm to 36 μm (Fig. 4d). By contrast, PPPB-M retained a comparatively smoother surface with only limited defect formation, and its mean Feret diameter decreased by 66%, from 407 μm to 139 μm . While specific stabilizer systems were not independently characterized, the observed difference suggests that transparent PPCT reaches an embrittled state at lower cumulative exposure than blue PPPB, indicating the formulation-level effects, such as the absence of UV-shielding pigments [64].

For the small size fraction (S, Fig. 4c), however, SEM imaging becomes less sensitive to surface features due to the resolution limit and contrast artifacts. Despite this limitation, particle size analysis showed that PPCT-S decreased 52%, from 94 μm to 45 μm , and PPPB-S decreased by 25%, from 109 μm to 82 μm (Fig. 4e), indicating that substantial fragmentation also happened in the smallest particles. Both PPCT and PPPB showed minimal observable changes in surface morphology at this scale, implying that aging in small particles primarily proceeds through the detachment of fine fragments rather than the formation of prominent cracks.

Statistical analysis (Fig. 4f–i, Mann–Whitney test) confirmed that all pre- vs. post-UVC size changes were significant ($p < 0.0001$). Although the maximum particle sizes remained high after aging (e.g., PPPB-M up to 847 μm), the bulk of each distribution shifted toward smaller sizes.

Overall, the morphological and particle size observations demonstrate that UVC-induced aging of PP is strongly influenced by both product origin and particle size. Large particles develop distinct crack networks whose characteristics depend on the formulation. In contrast, medium and small particles primarily reflect aging through a measurable reduction in particle size rather than through uniformly visible surface cracking.

Multidimensional Aspects of Polymer Aging

The results from our multi-technique approach (chemical, thermal, morphological) suggest that UVC-induced aging of PP proceeds through an interdependent cascade: surface oxidation weakens the polymer, which propagates into the bulk crystalline structure, ultimately facilitating fragmentation. This mechanistic view aligns with emerging experimental evidence that couples chemical alteration to physical disintegration under realistic aging conditions. For instance, Meides et al. reported that both stabilized and non-stabilized PP particles undergo exponential molecular-weight loss and produce large numbers of small particles under accelerated weathering [71]. Similarly, when bulk PP was exposed to natural seawater and environmental-like UV radiation, it released substantial quantities of secondary microplastics (50–5000 μm), far more than those produced by comparable

bio-based plastics under the same conditions [72]. In our experiments, the observed T_m depression and loss of χ_c for PP (especially in smaller particles) suggest that lamellar order is compromised early during aging. This structural destabilization likely underlies the transition from chemical modification to physical failure.

One plausible explanation for the polymer-specific differences in surface response is differential absorption of UVC (254 nm) light. Ultraviolet-Visible (UV-Vis) spectroscopy measurements on PP, PE, and PET thin films showed distinct absorbance behaviors under 254 nm irradiation [73], indicating polymer-type dependent spectral sensitivity. These differences in absorbance may influence the extent of surface degradation under UVC by modulating the amount of photon energy absorbed and made available to drive photochemical bond scission or subsequent oxidative reactions. However, this explanation should be treated with caution. In comparable experiments measuring microplastic formation under 254 nm irradiation, PP produced fewer particles than PET, indicating that absorption alone does not entirely dictate fragmentation [74]. In other words, while differential UVC absorption is likely a contributing factor to polymer-specific degradation, it is not the sole determinant—consistent with the broader understanding of polymer photodegradation processes [75].

Interestingly, the relationship between oxidation and fragmentation is not universal. In a recent study, environmental variables including humidity, temperature, and UV dose were evaluated across different polymer types. Although photo-oxidation is common, the generation of secondary micro- and nanoplastics depends strongly on both polymer identity and the aging conditions [76]. It is also shown that in the absence of mechanical stress, oxidation alone leads to only limited fragmentation [76, 77]. In addition, environmental matrices, such as catalytic (iron-bearing minerals), modulate degradation and may promote deeper oxidation, leading to more rapid progression to embrittlement and fracture beyond that observed in pure polymer [72, 78]. In practice, commercial PP items (e.g., colored or pigmented plastics) may thus age or fracture differently than unpigmented lab resins, complicating simple extrapolation from pristine materials.

Given the diversity of degradation pathways and outcomes, reliance on a single metric (e.g., carbonyl index) is insufficient to assess “how aged” a microplastic is, or its potential to fragment. Instead, the data and literature strongly support a multidimensional, integrated “aging score” approach that combines chemical (e.g., CI), thermal, structural (e.g., T_m , χ_c , χ_s), and morphological (e.g., particle size) indicators.

Aging Score: Correlation of Polymer Chemical, Thermal, Structural, and Morphological Properties

The diversity of measured properties highlights the multidimensional nature of microplastic aging. It raises the question of which metrics most reliably capture degradation/plastic aging, and whether they can be synthesized into a single, interpretable measure. Although fragmentation and size reduction are important aspects of microplastic aging, morphological metrics were not incorporated into the aging score in this study. The proposed aging score was intentionally defined using bulk, ensemble-averaged chemical and structural descriptors, while morphology reflects particle-level size distributions and can vary strongly with sampling and imaging conditions. Integrating these heterogeneous data types into a single score would require standardized distribution descriptors and different weighting strategies. Thus, only initial size, ΔT_m , ΔCI , $\Delta \chi_c$, and $\Delta \chi_s I$ were analyzed. Pearson correlation analysis (Fig. 5a) indicates that the initial particle size has minimal influence on the evolution of chemical, thermal, or structural properties, suggesting that surface and bulk responses are decoupled mainly from particle size within the studied range. The remaining measured quantities, or features, are observed to correlate with the cumulative UV dose (radiant exposure) and with one another. Changes in each feature relative to the control sample (ΔT_m , ΔCI , $\Delta \chi_c$, and $\Delta \chi_s I$) improve comparability across samples and strengthen correlations. Notably, CI and $\chi_s I$ are strongly positively correlated, with Pearson correlation coefficients (r) > 0.80 with respect to radiant exposure and with each other, reflecting the coupling between surface oxidation and near-surface crystallinity. In contrast,

T_m shows a stronger negative correlation with exposure ($r = -0.75$), whereas χ_c exhibits a weaker negative correlation ($r = -0.53$) and weaker correlations with other features, consistent with differential sensitivity of bulk crystallinity versus surface properties. Although both χ_c and $\chi_s I$ quantify crystallinity, they respond differently to UVC exposure: χ_c is negatively correlated, whereas $\chi_s I$ is positively correlated, due to the bulk versus surface sensitivity of the measurements.

Principal component analysis (PCA, Fig. 5b) reduces this multidimensional dataset to key axes of variance, with the first two components capturing $\sim 90\%$ of the variation. The first principal component (PC1) explains the most variance (in this case, 75%), with the second component (PC2) explaining less (15%), and the remaining components explain the remainder (Fig. S3). The weights of each feature toward each principal component (loading) also provide information about their importance (Fig. S3). The loading vectors shown in Fig. 5b indicate that T_m , CI , and $\chi_s I$ dominate the PC1, while χ_c contributes primarily to the PC2. The black star symbol in Fig. 5b represents the control samples, which collapse to a single point as each sample actually represents the difference from the control values. As the color gradient shows, samples with increased radiant exposure lie further from the control point, primarily along the PC1.

This can be utilized to establish a harmonized multivariate metric for the degree of aging in the sample. By measuring the distance of each sample from the control point in principal component space, we obtain an aging score that represents the overall change in properties (Fig. 5c). This distance is calculated as the weighted Euclidean distance, where directions along each principal component

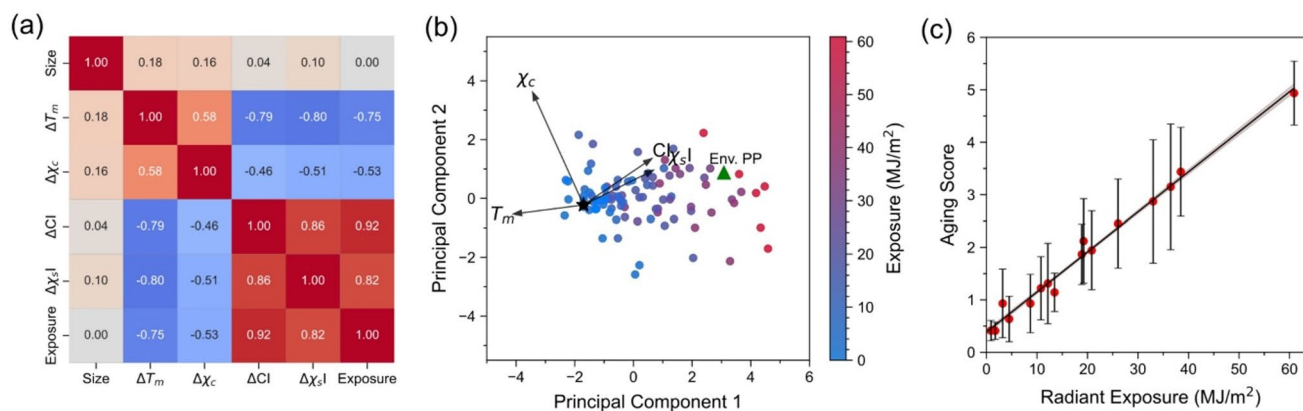
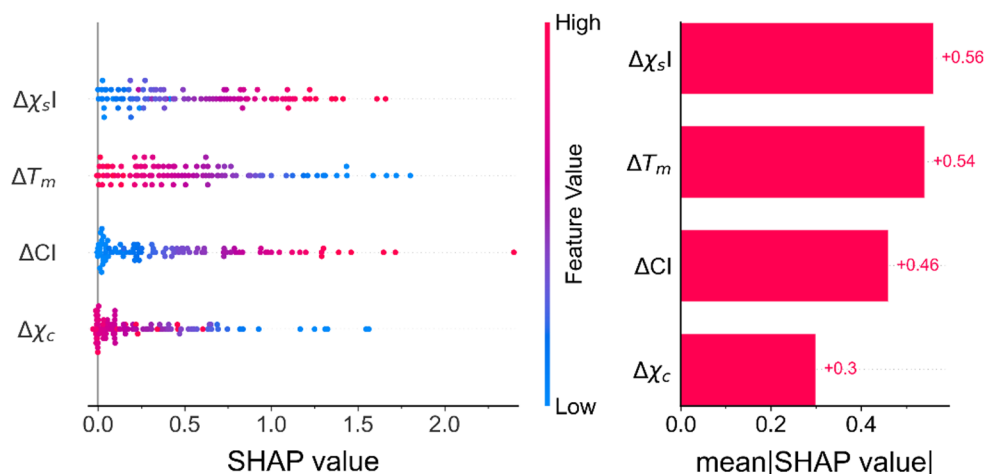


Fig. 5 Multidimensional analysis of PP microplastic aging metrics. **(a)** Pearson correlation matrix displaying the correlations among the initial size and changes in T_m , χ_c , CI , and $\chi_s I$. The color scale ranges from 1 (strong negative correlation) to 1 (strong positive correlation), with values near zero indicating no linear relationship. **(b)** Principal component analysis derived from χ_c , T_m , CI , and $\chi_s I$ for all PPPB and PPCT measurements, showing the first two principal components. Each point represents an individual sample, with the black star symbol representing the control sample.

Arrows show the loading vectors of the variables; their orientation and length reflect the direction and relative contribution of each property to the principal components. The Env. PP represents an environmental PP fragment that was not included in PCA model construction and serves as an independent application of the aging score. **(c)** An aging score is calculated as the weighted Euclidean distance from any point to the control point

Fig. 6 SHAP summary plot showing the contribution of different features ($\chi_s I$, T_m , CI, χ_c) to the aging score. Each point represents a sample, and the horizontal spread reflects the Shapley value, indicating the impact magnitude on the aging score. The right panel shows a SHAP bar plot ranking the average feature importance



are weighted by their explained variance. Weighting by explained variance ensures that poorly correlated or low-variance features have minimal impact on the score, while strongly correlated, high-variance features dominate. The resulting aging score exhibits a near-linear relationship with exposure time ($R^2 = 0.987$), providing a robust, predictive measure of cumulative degradation. It is noted that because the aging score is derived from multivariate relationships within a specific dataset, it is intended for comparative interpretation within a given experimental system rather than as an absolute metric transferable across studies without recalibration.

The contributions of individual features to the aging score were further evaluated using Shapley additive explanations (SHAP), which quantify the impact of each feature on the predicted score for every sample [79]. SHAP distributes the “total outcome” among all input variables according to their marginal contributions, and can be applied in a model-agnostic manner.

As shown in Fig. 6, the SHAP analysis largely agrees with the PCA results, confirming that χ_c is the least influential feature, with an average Shapley value of 0.3. Interestingly, CI receives a lower SHAP value than T_m and $\chi_s I$, despite having the strongest correlation with UVC exposure (Fig. 5a). This apparent discrepancy arises from the non-linear, sample-level sensitivity of each feature. At low exposure doses, CI shows minimal change and clusters near baseline values, resulting in smaller marginal contributions to the aging score [49]. In contrast, $\chi_s I$, which captures changes in surface crystallinity, and T_m , which reflects bulk thermal disruption, show more consistent contributions across the entire exposure range, giving them greater SHAP importance. A similar pattern is observed for χ_c , whose changes are modest relative to surface or thermal metrics.

The SHAP analysis thus provides complementary, mechanistic insight beyond PCA. While PCA emphasizes the features that contribute most to overall variance, SHAP

identifies which features actually drive the aging score on a per-sample basis. For instance, even if CI dominates variance across the dataset, its low sensitivity at early exposure levels reduces its impact for individual samples. By combining PCA and SHAP, we gain a more nuanced understanding of how chemical, thermal, and structural properties jointly govern the progression of microplastic aging. These results highlight that surface-sensitive metrics ($\chi_s I$) and bulk thermal indicators (T_m) are the most informative for predicting cumulative degradation, while bulk crystallinity (χ_c) plays a comparatively minor role.

Overall, the results (Fig. 6) emphasize the importance of integrating multiple complementary features into the aging score: features with different sensitivities and measurement depths contribute differently across the exposure spectrum, and SHAP allows us to quantify their relative contributions in a statistically robust, interpretable manner.

This aging score metric can also be applied to compare the previously measured commercial PE, PP, and PET powders and environmentally plastic waste samples (Fig. S4). The use of Δ features relative to the control facilitates the comparison of properties such as T_m and χ_c , which differences in initial polymer properties would otherwise confound. For some features, such as CI, differences in initial values across polymers cannot be entirely avoided; reference peaks were therefore selected to render CI values roughly comparable in scale. A surface-sensitive metric analogous to $\chi_s I$ could not be established for these plastics, so the analysis of multi-polymer datasets proceeded using three features (CI, T_m , and χ_c). This framework, however, is flexible and can accommodate any number of measured quantities. When applied to commercial plastic powders (PE, PP, and PET; Fig. S4), the PCA loadings and explained variance differ from the PP-only analysis (Fig. 5), reflecting intrinsic differences in feature variability across polymer types. Regardless of these differences, the overall aging score reproduces the same relative trends observed in Fig. 1: PP exhibits the most

significant increase in aging score relative to the control, followed by PE and PET at comparable, lower rates. These results demonstrate that the aging score provides a practical, quantitative summary of microplastic degradation and a general indication of the degree of aging across polymers.

The establishment of the aging score also provides a metric for the overall degree of aging in environmental samples. For instance, an environmentally sourced polypropylene fragment (Env. PP, green triangle, Fig. 5b) exhibited measured values of CI, T_m , χ_c , and $\chi_s I$ equal to 1.28, 142.8 °C, 43.3%, and 1.02, respectively, which fall within the range of the artificially aged PP samples. Since no dedicated control sample was available, the average values for each feature across all measured control samples were used to calculate Δ -values, enabling consistent comparison. The resulting aging score of 4.2 corresponds to approximately ~ 50 MJ m⁻² of UVC irradiation, demonstrating that this approach can contextualize environmental fragments relative to controlled laboratory aging. This also holds in the multi-polymer dataset, where environmental samples of PE and PP were found to have consistent degrees of aging to laboratory-aged samples (red and blue star symbols in Fig. S4a). With a sufficient number of environmental samples, this metric can be used to compare degrees of weathering across different samples, allowing quantitative assessment of variability in real-world polymer degradation. The reliability of such comparisons depends on the sample population, and artificially aged samples can serve as a calibration set to establish Δ -values and variance weights.

Taken together, the analyses in Figs. 5 and 6, and S4 illustrate how the various measurements shape the aging score. The correlation analysis highlights groups of properties that change in parallel, the PCA arranges these linked changes into significant variation patterns, and the SHAP analysis pinpoints each feature's contribution to the final score across samples. Both the multi-polymer comparison and the environmental fragment demonstrate how the framework handles differences in baseline properties and incomplete feature sets. These results define the operational behavior and practical boundaries of the aging score within the dataset used in this study, supporting its application as a descriptive tool for contextualizing environmental samples relative to aging.

Conclusion

This study elucidates the coupled chemical, structural, and physical degradation of polypropylene under UVC exposure, providing a mechanistic framework that connects surface oxidation, bulk lamellar destabilization, and particle fragmentation. Our analyses demonstrate that oxidative

modification at the polymer surface initiates a cascade of structural perturbations that propagate inward, weakening the bulk crystalline network and predisposing particles to mechanical failure. This mechanistic link is enhanced in smaller particles, where higher surface-to-volume ratios increase the contribution of surface oxidation to bulk destabilization. This emphasizes the role of particle geometry in degradation. Formulation-specific effects further modulate degradation pathways. Transparent PPCT particles, lacking UV-absorbing pigments, undergo finer and more continuous crack formation compared with blue PPPB, where stabilizers and colorants partially mitigate stress concentration and slow crack propagation. These observations underscore the role of additives in controlling both oxidative penetration and mechanical response, consistent with prior studies showing that polymer formulations can tune radical formation kinetics and energy dissipation.

Comparison with more UV-resistant polymers, such as PE and PET, confirms that backbone chemistry dictates the extent of bulk disruption; their semi-crystalline and aromatic structures confer resistance to lamellar disorder and fragmentation. This differential susceptibility emphasizes that laboratory UVC aging of PP cannot be extrapolated to all polymers without accounting for chemical structure, particle size, and formulation.

The integrated “aging score” approach developed here offers a robust, quantitative measure of cumulative degradation by combining chemical (i.e., CI), thermal, and structural (i.e., T_m , χ_c , $\chi_s I$), and morphological (i.e., particle size) metrics. By weighing features by variance and relevance, the aging score effectively summarizes multidimensional changes, enabling cross-comparison among particles of different sizes, formulations, and polymers. Strong correlations between the aging score and radiant exposure validate its potential as a predictive tool under diverse environmental conditions. The “aging score” concept, with further validation, may inform future studies on environmental microplastic formation, support standardization of laboratory aging protocols, and improve risk assessment strategies for polymer degradation in real-world settings.

Supplementary Information The online version contains supplementary material available at <https://doi.org/10.1007/s10924-026-03796-5>.

Acknowledgements The authors thank Dr. M. Chen for the discussion on the UVC setup.

Author contributions Y.L.: Conceptualization; Methodology; Investigation; Data Curation; Formal Analysis; Visualization; Writing – Original Draft, Review & Editing. D.P.: Investigation; Methodology; Data Curation; Formal Analysis; Visualization; Writing – Original Draft, Review & Editing. Z.J.: Methodology; Writing – Review & Editing. X.C.: Supervision; Investigation, Resources, Writing – Review & Editing. S.Z.: Supervision; Conceptualization; Methodology; Funding

Acquisition; Project Administration; Writing – Review & Editing.

Funding Open access funding provided by National Research Council Canada library. The authors appreciate the stipend support (Y.L.) of the Ocean Program at the National Research Council Canada (NRC) and the financial support from the Advancing a Circular Plastics Economy for Canada Program, funded by the Government of Canada.

Data Availability All data supporting the findings of this study are available within the paper and its Supplementary Information.

Declarations

Competing interests The authors declare no competing interests.

Open Access This article is licensed under a Creative Commons Attribution 4.0 International License, which permits use, sharing, adaptation, distribution and reproduction in any medium or format, as long as you give appropriate credit to the original author(s) and the source, provide a link to the Creative Commons licence, and indicate if changes were made. The images or other third party material in this article are included in the article's Creative Commons licence, unless indicated otherwise in a credit line to the material. If material is not included in the article's Creative Commons licence and your intended use is not permitted by statutory regulation or exceeds the permitted use, you will need to obtain permission directly from the copyright holder. To view a copy of this licence, visit <http://creativecommons.org/licenses/by/4.0/>.

References

- Liu S, Li L, Liu S, Liu L, Xiao X, Zhou D et al (2024) Reactive oxygen species-induced microplastics aging: Implications for environmental fate and ecological impact. *TrAC Trends Anal Chem* 173:117648. <https://doi.org/10.1016/j.trac.2024.117648>
- Castelvetto V, Corti A, Biale G, Ceccarini A, Degano I, La Nasa J et al (2021) New methodologies for the detection, identification, and quantification of microplastics and their environmental degradation by-products. *Environ Sci Pollut Res* 28(34):46764–46780. <https://doi.org/10.1007/s11356-021-12466-z>
- Shi Y, Shi L, Huang H, Ye K, Yang L, Wang Z et al (2024) Analysis of aged microplastics: a review. *Environ Chem Lett* 22(4):1861–1888. <https://doi.org/10.1007/s10311-024-01731-5>
- Baby MG, Gerritse J, Beltran-Sanahuja A, Wolter H, Rohais S, Romero-Sarmiento M-F (2025) Aging of plastics and microplastics in the environment: a review on influencing factors, quantification methods, challenges, and future perspectives. *Environ Sci Pollut Res* 32(3):1009–1042. <https://doi.org/10.1007/s11356-024-35651-2>
- Dimassi SN, Hahladakis JN, Yahia MND, Ahmad MI, Sayadi S, Al-Ghouti MA (2022) Degradation-fragmentation of marine plastic waste and their environmental implications: A critical review. *Arab J Chem* 15(11):104262. <https://doi.org/10.1016/j.arabjc.2022.104262>
- Tang L, Wu Q, Qu B (2005) The effects of chemical structure and synthesis method on photodegradation of polypropylene. *J Appl Polym Sci* 95(2):270–279. <https://doi.org/10.1002/app.21272>
- Beltrán-Sanahuja A, Casado-Coy N, Simó-Cabrera L, Sanz-Lázaro C (2020) Monitoring polymer degradation under different conditions in the marine environment. *Environ Pollut Res* 259:113836. <https://doi.org/10.1016/j.envpol.2019.113836>
- Xu Y, Ou Q, van der Hoek JP, Liu G, Lompe KM (2024) Photo-oxidation of Micro- and Nanoplastics: Physical, Chemical, and Biological Effects in Environments. *Environ Sci Technol* 58(2):991–1009. <https://doi.org/10.1021/acs.est.3c07035>
- Campanale C, Savino I, Massarelli C, Uricchio VF (2023) Fourier Transform Infrared Spectroscopy to Assess the Degree of Alteration of Artificially Aged and Environmentally Weathered Microplastics. *Polymers* 15(4):911. <https://doi.org/10.3390/polym15040911>
- Liu P, Shi Y, Wu X, Wang H, Huang H, Guo X et al (2021) Review of the artificially-accelerated aging technology and ecological risk of microplastics. *Sci Total Environ* 768:144969. <https://doi.org/10.1016/j.scitotenv.2021.144969>
- Hurtado Macias A, Román-Aguirre M, Talamantes RP, Soto KM, Reyes Araiza JL, Méndez-Lozano N et al (2024) Comparative study between UVB 313 nm, UVC 254 nm, and far UVC 222 nm light on the aging of polyamide 66. *Heliyon* 10(20):e39415. <https://doi.org/10.1016/j.heliyon.2024.e39415>
- Hijnen WAM, Beerendonk EF, Medema GJ (2006) Inactivation credit of UV radiation for viruses, bacteria and protozoan (oo) cysts in water: A review. *Water Res* 40(1):3–22. <https://doi.org/10.1016/j.watres.2005.10.030>
- Gao L, Su Y, Mehmood T, Wang Z, Peng L, Zhang N (2025) UVA-induced weathering of microplastics in seawater: surface property transformations and kinetics. *Front Mar Sci* 12:1519668. <https://doi.org/10.3389/fmars.2025.1519668>
- Galea J, Agius Anastasi A, Vella DA, Briffa SM (2025) UV Aging of PET Microplastics in a Custom-Built Weathering Chamber Replicating Mediterranean Conditions. *ACS Omega* 10(33):37486–37494. <https://doi.org/10.1021/acsomega.5c03491>
- Seghers J, Cella C, Pequeur E, La Spina R, Roncari F, Valsesia A et al (2025) Approaches for the preparation and evaluation of hydrophilic polyethylene and polyethylene terephthalate microplastic particles suited for toxicological effect studies. *Anal Bioanal Chem* 417(12):2589–2602. <https://doi.org/10.1007/s00216-024-05726-7>
- Jiang Y, Yin X, Xi X, Guan D, Sun H, Wang N (2021) Effect of surfactants on the transport of polyethylene and polypropylene microplastics in porous media. *Water Res* 196:117016. <https://doi.org/10.1016/j.watres.2021.117016>
- Andrady AL, Barnes PW, Bormann JF, Gouin T, Madronich S, White CC et al (2022) Oxidation and fragmentation of plastics in a changing environment; from UV-radiation to biological degradation. *Sci Total Environ* 851:158022. <https://doi.org/10.1016/j.scitotenv.2022.158022>
- Julienne F, Lagarde F, Delorme N (2019) Influence of the crystalline structure on the fragmentation of weathered polyolefines. *Polym Degrad Stab* 170:109012. <https://doi.org/10.1016/j.polymdegradstab.2019.109012>
- Rostampour S, Cook R, Jhang S-S, Li Y, Fan C, Sung L-P (2024) Changes in the Chemical Composition of Polyethylene Terephthalate under UV Radiation in Various Environmental Conditions. *Polymers* 16(16):2249. <https://doi.org/10.3390/polym16162249>
- Pinlova B, Nowack B (2024) From cracks to secondary microplastics - surface characterization of polyethylene terephthalate (PET) during weathering. *Chemosphere* 352:141305. <https://doi.org/10.1016/j.chemosphere.2024.141305>
- Su X, Liu M, Dai H, Dou J, Lu Z, Xu J et al (2024) Novel insight into the aging process of microplastics: An in-situ study in coastal wetlands. *Water Res* 248:120871. <https://doi.org/10.1016/j.watres.2023.120871>
- Li X, Huang D, Dong H, Wen J, Dong J, Zhang C et al (2024) Differential photoaging behaviors of different colored commercial polyethylene microplastics in water: The important role of color characteristics. *Sci Total Environ* 956:177361. <https://doi.org/10.1016/j.scitotenv.2024.177361>

23. Su J, Ruan J, Luo D, Wang J, Huang Z, Yang X et al (2023) Differential Photoaging Effects on Colored Nanoplastics in Aquatic Environments: Physicochemical Properties and Aggregation Kinetics. *Environ Sci Technol* 57(41):15656–15666. <https://doi.org/10.1021/acs.est.3c04808>
24. Li C, Jiang B, Guo J, Sun C, Shi C, Huang S et al (2022) Aging Process of Microplastics in the Aquatic Environments: Aging Pathway, Characteristic Change, Compound Effect, and Environmentally Persistent Free Radicals Formation. *Water* 14(21):3515. <https://doi.org/10.3390/w14213515>
25. Canopoli L, Coulon F, Wagland ST (2020) Degradation of excavated polyethylene and polypropylene waste from landfill. *Sci Total Environ* 698:134125. <https://doi.org/10.1016/j.scitotenv.2019.134125>
26. Kato Y, Carlsson DJ, Wiles DM (1969) The photo-oxidation of polypropylene: Some effects of molecular order. *J Appl Polym Sci* 13(7):1447–1458. <https://doi.org/10.1002/app.1969.070130708>
27. Carreiras-Suárez S, Domínguez-Ramos L, Lazzari M (2023) Study of the Long-Term Aging of Polypropylene-Made Disposable Surgical Masks and Filtering Facepiece Respirators. *Polymers* 15(4):1001. <https://doi.org/10.3390/polym15041001>
28. Rajakumar K, Sarasvathy V, Thamarai Chelvan A, Chitra R, Vijayakumar CT (2009) Natural Weathering Studies of Polypropylene. *J Polym Environ* 17(3):191–202. <https://doi.org/10.1007/s10924-009-0138-7>
29. Heinen W (1959) Infrared determination of the crystallinity of polypropylene. *J Polym Sci* 38(134):545–547. <https://doi.org/10.1002/pol.1959.1203813426>
30. Lanyi FJ, Wenzke N, Kaschta J, Schubert DW (2018) A method to reveal bulk and surface crystallinity of Polypropylene by FTIR spectroscopy - Suitable for fibers and nonwovens. *Polym Test* 71:49–55. <https://doi.org/10.1016/j.polymertesting.2018.08.018>
31. Wold S, Esbensen K, Geladi P (1987) Principal component analysis. *Chemom Intell Lab Syst* 2(1):37–52. [https://doi.org/10.1016/0169-7439\(87\)80084-9](https://doi.org/10.1016/0169-7439(87)80084-9)
32. Lukasiak BM, Zomer S, Brereton RG, Faria R, Duncan JC (2007) Pattern recognition and feature selection for the discrimination between grades of commercial plastics. *Chemom Intell Lab Syst* 87(1):18–25. <https://doi.org/10.1016/j.chemolab.2006.01.003>
33. Mitchell G, France F, Nordon A, Tang PL, Gibson LT (2013) Assessment of historical polymers using attenuated total reflectance-Fourier transform infra-red spectroscopy with principal component analysis. *Herit Sci* 1(1):28. <https://doi.org/10.1186/2050-7445-1-28>
34. Watanabe R, Nakamura S, Sugahara A, Kishi M, Sato H, Hagiwara H et al (2024) Revealing Molecular-Scale Structural Changes in Polymer Nanocomposites during Thermo-Oxidative Degradation Using Evolved Gas Analysis with High-Resolution Time-of-Flight Mass Spectrometry Combined with Principal Component Analysis and Kendrick Mass Defect Analysis. *Anal Chem* 96(6):2628–2636. <https://doi.org/10.1021/acs.analchem.3c05269>
35. Song D, Gao J, Li X, Lu L (2014) Evaluation of aging behavior of polypropylene in natural environment by principal component analysis. *Polym Test* 33:131–137. <https://doi.org/10.1016/j.polymertesting.2013.11.014>
36. Qin L, Zhu Y, Liu S, Zhang X, Zhao Y (2025) The Shapley Value in Data Science: Advances in Computation, Extensions, and Applications. *Mathematics* 13(10):1581. <https://doi.org/10.3390/math13101581>
37. Yao J, Qian H, Yan Z, Zhao X, Gao N, Zhang Z (2024) Insight into the effect of UVC-based advanced oxidation processes on the interaction of typical microplastics and their derived disinfection byproducts during disinfection. *J Hazard Mater* 472:134597. <https://doi.org/10.1016/j.jhazmat.2024.134597>
38. Lin J, Yan D, Fu J, Chen Y, Ou H (2020) Ultraviolet-C and vacuum ultraviolet inducing surface degradation of microplastics. *Water Res* 186:116360. <https://doi.org/10.1016/j.watres.2020.116360>
39. Diepens M, Gijsman P (2011) Outdoor and accelerated weathering studies of bisphenol A polycarbonate. *Polym Degrad Stab* 96(4):649–652. <https://doi.org/10.1016/j.polymdegradstab.2010.12.009>
40. Andrady AL, Heikkilä AM, Pandey KK, Bruckman LS, White CC, Zhu M et al (2023) Effects of UV radiation on natural and synthetic materials. *Photochem Photobiol Sci* 22(5):1177–1202. <https://doi.org/10.1007/s43630-023-00377-6>
41. Rostampour S, Jhang SS, Hsu J-K, Cook R, Li Y, Fan C et al (2025) Evaluating the Environmental Factors on Microplastic Generation: An Accelerated Weathering Study. *Microplastics* 4(1):13. <https://doi.org/10.3390/microplastics4010013>
42. Syranidou E, Karkanorachaki K, Barouta D, Papadaki E, Moschovas D, Avgeropoulos A et al (2023) Relationship between the Carbonyl Index (CI) and Fragmentation of Polyolefin Plastics during Aging. *Environ Sci Technol* 57(21):8130–8138. <https://doi.org/10.1021/acs.est.3c01430>
43. Knopp MM, Löbmann K, Elder DP, Rades T, Holm R (2016) Recent advances and potential applications of modulated differential scanning calorimetry (mDSC) in drug development. *Eur J Pharm Sci* 87:164–173. <https://doi.org/10.1016/j.ejps.2015.12.024>
44. Leng Y, Gaburici L, Cao X, Zou S (2025) Quantification of microplastics in complex environmental matrices using a tiered approach with modulated differential scanning calorimetry (MDSC). *Anal Bioanal Chem*. <https://doi.org/10.1007/s00216-025-06212-4>
45. Blaine RL (2002) Thermal Applications Note: Polymer Heats of Fusion. TA Instruments. www.tainstruments.com/pdf/literature/TN048.pdf
46. Baek S-J, Park A, Ahn Y-J, Choo J (2015) Baseline correction using asymmetrically reweighted penalized least squares smoothing. *Analyst* 140(1):250–257. <https://doi.org/10.1039/C4AN01061B>
47. Erb D (2022) Pybaselines: A Python Library of Algorithms for the Baseline Correction of Experimental Data. <https://doi.org/10.5281/zenodo.10676584>
48. Miranda MN, Sampaio MJ, Tavares PB, Silva AMT, Pereira MFR (2021) Aging assessment of microplastics (LDPE, PET and uPVC) under urban environment stressors. *Sci Total Environ* 796:148914. <https://doi.org/10.1016/j.scitotenv.2021.148914>
49. Rouillon C, Bussiere PO, Desnoux E, Collin S, Vial C, Therias S et al (2016) Is carbonyl index a quantitative probe to monitor polypropylene photodegradation? *Polym Degrad Stab* 128:200–208. <https://doi.org/10.1016/j.polymdegradstab.2015.12.011>
50. García-López EI, Aoun N, Marci G (2024) An Overview of the Sustainable Depolymerization/Degradation of Polypropylene Microplastics by Advanced Oxidation Technologies. *Molecules* 29(12):2816. <https://doi.org/10.3390/molecules29122816>
51. Chamas A, Moon H, Zheng J, Qiu Y, Tabassum T, Jang JH et al (2020) Degradation Rates of Plastics in the Environment. *ACS Sustain Chem Eng* 8(9):3494–3511. <https://doi.org/10.1021/acssuschemeng.9b06635>
52. Abang S, Wong F, Sarbatly R, Sariau J, Bains R, Besar NA (2023) Bioplastic classifications and innovations in antibacterial, antifungal, and antioxidant applications. *J Bioresour Bioprod* 8(4):361–387. <https://doi.org/10.1016/j.jobab.2023.06.005>
53. Khairul Anuar NFS, Huyop F, Ur-Rehman G, Abdullah F, Normi YM, Sabullah MK et al (2022) An Overview into Polyethylene Terephthalate (PET) Hydrolases and Efforts in Tailoring Enzymes for Improved Plastic Degradation. *Int J Mol Sci* 23(20):12644. <https://doi.org/10.3390/ijms232012644>

54. Höhne GWH, Hemminger WF, Flammersheim HJ (2003) Applications of Differential Scanning Calorimetry. In: Höhne GWH, Hemminger WF, Flammersheim HJ (eds) *Differential Scanning Calorimetry*. Springer, Berlin, Heidelberg, pp 147–244. https://doi.org/10.1007/978-3-662-06710-9_6
55. Chiapasco M, Valsecchi M, Hill G, Wallis C, Porter AE, Giuliani F (2025) Impacts of Photooxidation on Commercially Available Homo and Copolymers of Polypropylene on Their Microstructure and Mechanics: A Cross-Sectional Analysis. *Nano Select* 6(1):e202300082. <https://doi.org/10.1002/nano.202300082>
56. Rabello MS, White JR (1997) Crystallization and melting behaviour of photodegraded polypropylene — I. Chemi-crystallization. *Polymer* 38(26):6379–6387. [https://doi.org/10.1016/S0032-3861\(97\)00213-9](https://doi.org/10.1016/S0032-3861(97)00213-9)
57. Wu X, Zhao X, Chen R, Liu P, Liang W, Wang J et al (2023) Size-dependent long-term weathering converting floating polypropylene macro- and microplastics into nanoplastics in coastal seawater environments. *Water Res* 242:120165. <https://doi.org/10.1016/j.watres.2023.120165>
58. Bonifazi G, Fiore L, Pelosi C, Serranti S (2023) Evaluation of plastic packaging waste degradation in seawater and simulated solar radiation by spectroscopic techniques. *Polym Degrad Stab* 207:110215. <https://doi.org/10.1016/j.polymdegradstab.2022.110215>
59. Cai L, Wang J, Peng J, Wu Z, Tan X (2018) Observation of the degradation of three types of plastic pellets exposed to UV irradiation in three different environments. *Sci Total Environ* 628–629:740–747. <https://doi.org/10.1016/j.scitotenv.2018.02.079>
60. Hoseini M, Stead J, Bond T (2023) Ranking the accelerated weathering of plastic polymers. *Environ Sci Process Impacts* 25(12):2081–2091. <https://doi.org/10.1039/D3EM00295K>
61. Gijsman P, Meijers G, Vitarelli G (1999) Comparison of the UV-degradation chemistry of polypropylene, polyethylene, polyamide 6 and polybutylene terephthalate. *Polym Degrad Stab* 65(3):433–441. [https://doi.org/10.1016/S0141-3910\(99\)00033-6](https://doi.org/10.1016/S0141-3910(99)00033-6)
62. Hahladakis JN, Velis CA, Weber R, Iacovidou E, Purnell P (2018) An overview of chemical additives present in plastics: Migration, release, fate and environmental impact during their use, disposal and recycling. *J Hazard Mater* 344:179–199. <https://doi.org/10.1016/j.jhazmat.2017.10.014>
63. Dimassi SN, Hahladakis JN, Daly Yahia MN, Ahmad MI, Sayadi S, Al-Ghouti MA (2023) Insights into the degradation mechanism of PET and PP under marine conditions using FTIR. *J Hazard Mater* 447:130796. <https://doi.org/10.1016/j.jhazmat.2023.130796>
64. Key S, Ryan PG, Gabbott SE, Allen J, Abbott AP (2024) Influence of colourants on environmental degradation of plastic litter. *Environ Pollut* 347:123701. <https://doi.org/10.1016/j.envpol.2024.123701>
65. Xue Z, Yu X, Ke X, Zhao J (2024) A novel route for microplastic mineralization: visible-light-driven heterogeneous photocatalysis and photothermal Fenton-like reaction. *Environ Sci Nano* 11(1):113–122. <https://doi.org/10.1039/D3EN00642E>
66. Born MP, Brüll C, Schüttrumpf H (2023) Implications of a New Test Facility for Fragmentation Investigations on Virgin (Micro)plastics. *Environ Sci Technol* 57(28):10393–10403. <https://doi.org/10.1021/acs.est.3c02189>
67. Wu H, Zhao Y, Dong X, Su L, Wang K, Wang D (2021) Probing into the microstructural evolution of isotactic polypropylene during photo-oxidation degradation. *Polym Degrad Stab* 183:109434. <https://doi.org/10.1016/j.polymdegradstab.2020.10.9434>
68. Boronat C, Correcher V, García-Guinea J, Bravo-Yagüe JC (2024) Ultraviolet C radiation on polypropylene: A potential way to reduce plastic pollution. *Polym Degrad Stab* 225:110784. <https://doi.org/10.1016/j.polymdegradstab.2024.110784>
69. Delbruel V, Lajoie H, Steiner V, Gérard J-F, Duchet-Rumeau J, Chevalier J (2024) Effects of polypropylene compositions and processing conditions on its aging resistance under tropical environments. *Polym Degrad Stab* 228:110883. <https://doi.org/10.1016/j.polymdegradstab.2024.110883>
70. Turton TJ, White JR (2001) Effect of stabilizer and pigment on photo-degradation depth profiles in polypropylene. *Polym Degrad Stab* 74(3):559–568. [https://doi.org/10.1016/S0141-3910\(01\)00193-8](https://doi.org/10.1016/S0141-3910(01)00193-8)
71. Meides N, Mauer A, Menzel T, Altstädt V, Ruckdäschel H, Senker J et al (2022) Quantifying the fragmentation of polypropylene upon exposure to accelerated weathering. *Microplast Nanoplast* 2(1):23. <https://doi.org/10.1186/s43591-022-00042-2>
72. Niu Z, Curto M, Le Gall M, Demeyer E, Asselman J, Janssen CR et al (2024) Accelerated fragmentation of two thermoplastics (polylactic acid and polypropylene) into microplastics after UV radiation and seawater immersion. *Ecotoxicol Environ Saf* 271:115981. <https://doi.org/10.1016/j.ecoenv.2024.115981>
73. Hebner TS, Maurer-Jones MA (2020) Characterizing microplastic size and morphology of photodegraded polymers placed in simulated moving water conditions. *Environ Sci Process Impacts* 22(2):398–407. <https://doi.org/10.1039/C9EM00475K>
74. Mikac L, Csáki A, Zentai B, Rigó I, Veres M, Tolić A et al (2024) UV Irradiation of Polyethylene Terephthalate and Polypropylene and Detection of Formed Microplastic Particles Down to 1 µm. *ChemPlusChem* 89(2):e202300497. <https://doi.org/10.1002/cplu.202300497>
75. Suh D, Hockett Sherlock S, Dukes KC, Perencevich EN, Marra AR (2025) Impact of UV-C on material degradation: a scoping literature review. *Antimicrob Steward Healthc Epidemiol* 5(1):e199. <https://doi.org/10.1017/ash.2025.10114>
76. Pfohl P, Santizo K, Sipe J, Wiesner M, Harrison S, Svendsen C et al (2025) Environmental degradation and fragmentation of microplastics: dependence on polymer type, humidity, UV dose and temperature. *Microplast Nanoplast* 5(1):7. <https://doi.org/10.1186/s43591-025-00118-9>
77. Polruang S, Asokbunyarat V, Bouthong P, Rizqa F, Somprasong A (2025) Simulated environmental weathering of expanded polystyrene foam and polypropylene under UV and wave agitation. *Sci Rep* 15(1):38649. <https://doi.org/10.1038/s41598-025-22367-7>
78. Song YK, Hong SH, Eo S, Shim WJ (2023) Fragmentation of nano- and microplastics from virgin- and additive-containing polypropylene by accelerated photooxidation. *Environ Pollut* 327:121590. <https://doi.org/10.1016/j.envpol.2023.121590>
79. Lundberg SM, Lee S-I (2017) A Unified Approach to Interpreting Model Predictions. In: 31st Conference on Neural Information Processing Systems (NIPS 2017), Long Beach, CA, USA. <https://doi.org/10.48550/arXiv.1705.07874>